Investigation of the Influence of Nanostructured $LiNi_{0.33}Co_{0.33}Mn_{0.33}O_2$ Lithium-Ion Battery Electrodes on Performance and Aging

Andreas M. Dreizler,[1,z] Nicole Bohn,[2] Holger Geßwein,[2] Marcus Müller,[2] Joachim R. Binder,[2] Norbert Wagner,[1] and K. Andreas Friedrich[1,3,*]

[1]*German Aerospace Center (DLR), Institute of Engineering Thermodynamics, 70569 Stuttgart, Germany*
[2]*Karlsruhe Institute of Technology (KIT), Institute for Applied Materials (IAM-KWT), 76344 Eggenstein-Leopoldshafen, Germany*
[3]*University of Stuttgart, Institute for Energy Storage, 70569 Stuttgart, Germany*

The paper focuses on the performance and aging behavior of lithium nickel cobalt manganese oxide commercial standard material (NCM-111) which is improved with a post synthesis process in order to enhance the cathode active material of lithium-ion pouch cells regarding their capacity and cyclic stability. The aging behavior of the cells is analyzed with electrochemical impedance spectroscopy (EIS) during long-term electrochemical load cycling tests based on the Common Artemis Driving Cycle (CADC). Additionally, post-mortem investigations using scanning electron microscopy (SEM) and X-ray diffraction (XRD) were performed. The results demonstrate that post-processing of electrode active material is an effective tool to improve the properties of lithium-ion electrode materials, especially regarding high energy applications and lifetime optimization. The paper bridges the gap between lithium-ion battery electrode material development and the necessary cell testing under automotive relevant conditions which is important for the evaluation of new lithium-ion battery materials for automotive applications.

© The Author(s) 2018. Published by ECS. This is an open access article distributed under the terms of the Creative Commons Attribution Non-Commercial No Derivatives 4.0 License (CC BY-NC-ND, http://creativecommons.org/licenses/by-nc-nd/4.0/), which permits non-commercial reuse, distribution, and reproduction in any medium, provided the original work is not changed in any way and is properly cited. For permission for commercial reuse, please email: oa@electrochem.org. [DOI: 10.1149/2.1061802jes]

Manuscript submitted November 20, 2017; revised manuscript received January 10, 2018. Published January 24, 2018.

Electrification is the most viable solution to achieve clean and efficient transportation, especially in large towns and cities, to significantly reduce harmful greenhouse gases and fine dust.[1] Lithium-ion batteries deliver an unmatched combination of high energy and power density, making it the technology of choice for portable electronic devices, power tools and electric vehicles including (hybrid electric vehicles (HEVs), plug-in hybrid electric vehicles (PHEVs), and pure battery electric vehicles (BEVs).[2,3] Particularly with regard to automotive applications high energy lithium-ion batteries that are cycle resistant are essential to obtain acceptable vehicle ranges. Beside high capacity, the main requirements for cathode materials must include long cycle lifetime, high thermal stability and fast charging capability.[4]

Lithium nickel cobalt manganese oxide ($LiNi_xCo_yMn_zO_2$; $x + y + z = 1$; NCM) is the current state-of-the-art cathode electrode material in lithium-ion batteries for mobile applications, whereby $LiNi_{0.33}Co_{0.33}Mn_{0.33}O_2$ (NCM-111) is currently the most common form of NCM and is widely used in the battery market.[3] For this purpose, numerous research studies are presently concentrating on the improvement of NCM electrode materials for lithium-ion batteries. In principle, cathode materials for lithium-ion batteries can be improved in various ways to achieve an enhancement of thermal, mechanical, and chemical stability as well as electronic and ionic conductivity, e.g. by variation of the chemical composition[5] or by the optimization of the morphology.[6] Thus, some recent efforts, such as formation of macroporous NCM, exhibit high reversible specific cell capacities and good cycle stability even at an enhanced temperature of 50°C.[7] Nevertheless, some challenges remain for NCM cathodes, including the intrinsic low lithium-ion conductivity and the still unsatisfying thermal stability.[4]

The aim of this work is to use a commercial standard material and to process it in an easy way in order to improve the cathode material properties regarding the cell capacity and cycle lifetime. Due to the high relevance of mobile transportation and automotive applications, it is straightforward to perform a long-term stress test based on a state of the art driving cycle test for cars and other vehicles. For this investigation the Common Artemis Driving Cycle (CDAC) was selected and the electrical long-term load cycling test was carried out with the in-house processed nanostructured NCM cathode materials. Different lithium-ion pouch cells with conventional and nanostructured NCM electrodes were tested with regards to cell capacity and cycle stability within the load cycling test. The experiment is complemented by a periodically performed electrochemical impedance spectroscopy investigation, in addition to a detailed post-mortem analysis of the cathode electrodes after the experiment.

Experimental

Common artemis driving cycle.—The Common Artemis Driving Cycle (CADC) was developed within the European Artemis (Assessment and Reliability of Transport Emission Models and Inventory Systems) project in order to test the emission characteristics of fossil fuel vehicles. This emission test includes three different driving schedules: urban, rural road and motorway. The motorway cycle has two variants with maximum speeds of 130 and 150 km h^{-1}.[8–10]

In this work, the urban profile of the CADC is used to simulate an automotive relevant characteristic to test cell ageing under load conditions of lithium-ion pouch batteries.

Fig. 1 illustrates the related velocity and acceleration over the time. The urban driving cycle lasts 920 s, has an average speed of 17.5 km h^{-1} and corresponds to a driving distance of 4.47 km, while the maximum speed is 58 km h^{-1}. Furthermore, it includes traffic light phases in terms of start-stop cycles.[11]

The driving profile contains positive and negative accelerations. In relation to an automotive lithium-ion battery or to an electrical vehicle that includes a battery pack, a positive acceleration means discharging, while a negative acceleration is a recharging process to simulate the energy recuperation of the vehicle during braking phases.

Load cycling and electrochemical impedance spectroscopy.—Load cycling of the pouch cells is done using a commercial battery test system from BaSyTec (12 V, 16 A, 200 W) in a climatic chamber at 23°C. The impedance test system IM6 is from ZAHNER-elektrik GmbH & Co. KG.

The batteries are stressed according to the Common Artemis Driving Cycle introduced above in the urban profile at ambient temperature. In order to relate the velocity and acceleration data to battery

*Electrochemical Society Member.
[z]E-mail: Andreas.Dreizler@dlr.de

Downloaded on 2019-04-15 to IP 178.251.91.98 address. Redistribution subject to ECS terms of use (see ecsdl.org/site/terms_use) unless CC License in place (see abstract).

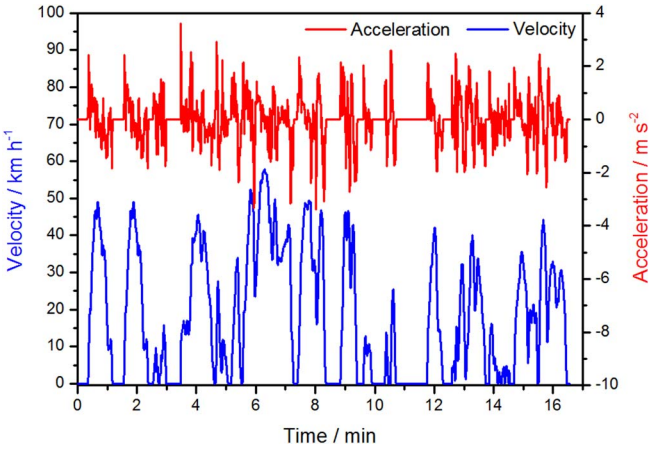

Figure 1. Urban characteristics of the Common Artemis Driving Cycle.

current values, a Modelica simulation of the city car "Hotzenblitz" which is a limited-lot production vehicle was used. This vehicle is equipped with a 12 kW electric traction drive and reaches a maximum speed of 112 km h^{-1}. For the simulation, a bigger 30 kW traction motor was assumed to fulfill the applied driving cycles. Afterwards, the whole driving cycle data was adjusted to the pouch cell capacity and was scaled to guarantee that the battery current during the peak loads lies in the range between 2 and 3 C.

During load cycling the battery loses capacity since it will be considerably more discharged than charged. Therefore, the maximum number of cycles is limited. The battery is operated between 3.0 V (end-point voltage) and 4.2 V (charging end voltage). The charging routine is constant current (CC) without an additional constant voltage (CV) step. During the test, the pouch cell will be stressed between the state of charge (SOC) window of 10 and 90% (SOC10 and SOC90). For both states, the abortion criteria during load cycling are the corresponding cell voltages for SOC10 and SOC90 that are determined in an initial test. They are in the range from 3.43 to 3.45 V for SOC10 and 3.98 to 4.05 V for SOC90. The state of health (SOH) will be calculated between SOC0 (3.0 V) and SOC100 (4.2 V) at a defined point in time, usually after 100 CADCs, and refers to the ratio of actually determined discharge capacity and capacity at the test start.

At the beginning of the test, the initial state of the battery (SOC90) is ensured by either charging or discharging the battery with a C/5 current. The initial state of SOC90 guarantees that the battery will not be overcharged during load cycling. After one urban CADC, a five minute waiting period follows. In this respect, three scenarios are implemented in the test procedure:

1. If the cell voltage is higher than the cell voltage at SOC10 after less than 100 load cycles, a further driving cycle will be performed.
2. If the actual cell voltage is equal or less the SOC10 cell voltage and the amount of 100 load cycles is not reached, the battery initial state will be recovered ($I = \pm C/5$ until SOC90). The lowest state of charge during the experiment is 10% in order to prevent the battery from deep discharging.
3. If the amount of 100 driving cycles is reached, the initial state (SOC50) for electrochemical impedance spectroscopy (EIS) is established by either charging or discharging the battery with C/5.

Since the impedance of a battery depends on the SOC level, the same charge condition must always be reached for EIS. SOC50 has been chosen as initial state for the EIS measurements to prevent the battery from overcharging and deep discharging considering that the impedance spectrometer applies a current to the battery cell.

Generally, the EIS experiments are carried out in potentiostatic mode by applying a voltage signal with 5 mV amplitude in the frequency range of 10 mHz to 4 MHz, while the initial point is 1 kHz. After each EIS measurement the original battery SOC is restored to provide the start position for the next load cycle. To ensure that a constant connecting resistance between EIS cables and both current collectors is maintained, the electrical contact is realized with a screw-retained pressure contact fixture instead of crocodile clips.

Powder processing and characterization.—For the comparison of dense lithium nickel cobalt manganese oxide (NCM) powders and corresponding nanostructured materials, a commercially available $LiNi_{0.33}Co_{0.33}Mn_{0.33}O_2$ powder (NM-3100, Toda America) was used. This as received NCM (p-NCM) powder – denominated pristine – was milled and dispersed in distilled water for 3.5 h using an agitator bead mill (LabStar LS1, Netzsch) with yttria-stabilized zirconia beads (diameter: 0.2 mm). The suspension contains 25 wt% NCM powder and 1.6 wt% Darvan 821A (Vanderbilt Minerals) as dispersant. After milling 0.25 wt% polyethylene glycol (Sigma Aldrich) was added and the suspension was spray-dried (MobileMinor, GEA Niro). The spray-dried NCM granules were calcined at 900°C for 5 h (heating rate 5 K min^{-1}) under air in an alumina crucible and yielded a nanostructured NCM (n-NCM) powder.

The specific surface area (A_{BET}) of the pristine and nanostructured NCM powders was measured by nitrogen adsorption method (Gemini VII 2390, Micrometrics). With the measured specific surface area and the theoretical density ρ of NCM (4.77 $g \cdot cm^{-3}$)[12] the primary particle diameter can be calculated with $d_{BET} = 6/(\rho \cdot A_{BET})$. The morphology and the microstructure of the powders were studied by using a field emission scanning electron microscope (Supra 55, Zeiss) with an accelerating voltage of 10 kV. The primary particle size distribution d_{SEM} was determined by image analysis of SEM micrographs (imageJ Software). Therefore, the largest diameter of two boundary points of the particle was measured. For each powder at least 200 primary particles were analyzed. To investigate the microstructure of the NCM granules, cross-sections of corresponding electrode films were prepared by using an ion beam milling system (EM TIC3X triple ion beam cutter, Leica Mikrosysteme). The process was performed under vacuum with an accelerating voltage of 6 kV for the argon ions, 2.2 mA gun current and a period of 6 h.

The granule size distribution was measured by laser diffraction (Horiba LA950, Retsch Technology), and pore size distribution was investigated by mercury intrusion porosimetry (CEI Pascal 1.05, Thermo Electron). The relative porosity P of the NCM granules can be calculated after $P = V_P/(V_P + 1/\rho)$ using the measured specific pore volume V_P for pore widths < 400 nm.

Electrodes preparation and pouch cell assembling.—Cathode electrodes were produced by using the commercial p-NCM powder and the modified n-NCM powder, respectively. Therefore, polyvinylidene difluoride (PVDF) binder (Solef 5130, Solvay Solexis), carbon black (Super C65, Imerys Graphite & Carbon), graphite (KS6L Imerys Graphite & Carbon), and NCM powder were dispersed in N-methyl-2-pyrrolidone (Sigma Aldrich) using a vacuum equipped dissolver (VMA Getzmann) with a maximum speed of 2000 rpm for 1 h. The resulting slurries contain approximately 87 wt% NCM, 5 wt% graphite, 4 wt% carbon black, and 4 wt% PVDF binder. The electrode sheets were prepared by casting the slurries onto a 20 μm thick aluminum foil using a continuous laboratory coater (KTF-S, Mathis) equipped with doctor-blade technology and convection dryer. By adjusting the gap of the doctor blade (180 μm and 360 μm), the active material loading of the electrodes were set to 12 $mg \cdot cm^{-2}$ and 24 $mg \cdot cm^{-2}$, respectively. In order to obtain comparable volumetric loading densities, the electrodes with n-NCM powder were slightly compacted after drying.

Commercial graphite (SMG-A, Hitachi Chemical) was used as active material for the anodes. Additional components of the electrodes are sodium carboxymethyl cellulose (WALOCEL CRT 2000 PA07, Dow Wolf), SBR-latex binder (TRD 2001, JSR Micro), and carbon black (C-NERGY C65, Imerys Graphite & Carbon). The electrode sheets were prepared by casting aqueous slurries onto a 10 μm thick copper foil using also a continuous laboratory coater (KTF-S, Mathis AG). The active material loading of the electrodes were set to 7 $mg \cdot cm^{-2}$ and 13 $mg \cdot cm^{-2}$ and the sheets were calendered to a

Downloaded on 2019-04-15 to IP 178.251.91.98 address. Redistribution subject to ECS terms of use (see ecsdl.org/site/terms_use) unless CC License in place (see abstract).

Table I. Specifications for the pouch cells made with nickel cobalt manganese oxide (cathode) and graphite electrodes (anode).

	Cathode				Anode		
Pouch cell type	Active material	Active material loading/mg · cm^{-2}	Electrode thickness/μm	Electrode porosity/%	Active material loading/mg · cm^{-2}	Electrode thickness/μm	Electrode porosity/%
PC-12p	p-NCM	12.2	74	53	7.2	58	38
PC-24p	p-NCM	24.6	152	54	13.2	125	47
PC-12n	n-NCM	12.2	73	52	7.2	58	38
PC-24n	n-NCM	25.2	154	53	13.2	125	47

porosity of 47% and 38%, respectively. The composition of the dried electrodes is as follows: 93 wt% graphite, 2 wt% carbon black, 2 wt% Na-CMC, and 3 wt% SBR.

Pouch cells with ceramic coated separator foil (Separion, Evonik) and electrolyte consisting of EC:DMC at a ratio of 1:1 and 1 M $LiPF_6$ (LP30, BASF) were prepared for the electrochemical tests. Electrode size was 50 × 50 mm^2 for the cathode and 54 × 54 mm^2 for the anode. Before assembling, all electrodes and separators were dried overnight in a vacuum furnace at 130°C. After assembling in a dry room, all cells were stored around 20 h at 40°C to facilitate a homogeneous distribution of the electrolyte within the electrodes. All cells were formed by going through two cycles at 0.05 C charging and discharging rates. Cycling voltage limits were set at the first cycle from 3.0 V and 4.1 V and the second cycles from 3.0 V and 4.2 V.

The technical specifications of the pouch cells and electrodes are listed in Table I. The porosity of the electrodes P_e was calculated through the determined active material loading L_{am} and the measured electrode thickness d_e, the mass fraction of the active material x_{am} and the theoretical density of the electrode materials ρ_{em} after $P_e = 1–L_{am}/(d_e \cdot x_{am} \cdot \rho_{em})$. The theoretical densities of the cathode and anode electrode materials are 4.01 g cm^{-3} and 2.16 g cm^{-3}, respectively.

The electrode thickness was measured by means of SEM images using the cross section of the electrode films (preparation sees above). X-ray diffraction patterns of the electrode before and after load cycling were recorded with a powder diffractometer (D5000, Siemens; Cu-$K_{\alpha1,2}$ radiation). Measurements were performed in the 2θ range between 15 and 80° with a step size of 0.04° and a dwell time of 4 s per step. The post mortem analysis of the cathode electrodes was carried out by scanning electron microscopy and X-ray diffraction.

Results and Discussion

Cathode powder properties.—Four different types of pouch cells, as introduced in the Experimental section, were tested regarding their aging behavior during the Artemis Urban Driving Cycle. Beside the variation of the loading density of the electrodes, the influence of the morphology and microstructure of the cathode materials was investigated. SEM micrographs (Fig. 2) of conventional NCM (p-NCM) and nanostructured NCM (n-NCM) materials illustrate the morphology of the powder before and after the nanostructuring procedure. By milling of the p-NCM to a mean particle size of 0.2 μm and subsequent spray-drying and calcination uniform, homogeneous and spherical granules are formed. The median diameter $d_{50,3}$ is 16.4 μm for n-NCM and 9.3 μm for p-NCM, respectively. The primary particles of n-NCM are also more uniform and additionally smaller (d_{SEM} value: 0.46 μm) than the primary particles of p-NCM (d_{SEM} value: 0.83 μm). Hence, the specific surface area of the n-NCM material is with 2.52 m^2 g^{-1} seven times larger than the surface area of the p-NCM powder. The primary particle sizes – calculated from the BET values (d_{BET}) and from the SEM images (d_{SEM}) – are comparably for the n-NCM powder. The difference between the calculated primary particle sizes for the p-NCM powder result from the distinct sintering necks and the partly closed porosity of the secondary particles. The p-NCM powders are nearly dense; whereas the spray-dried n-NCM powder has an open porosity of 40.6% (Fig. 2, right). This ensures a better wettability relating to penetration through the electrolyte. The properties of the two powders are summarized in Table II.

Artemis urban load cycling test.—The electrodes were tested regarding their aging behavior during the Artemis Urban Driving Cycle. The cell degradation was monitored by means of electrochemical

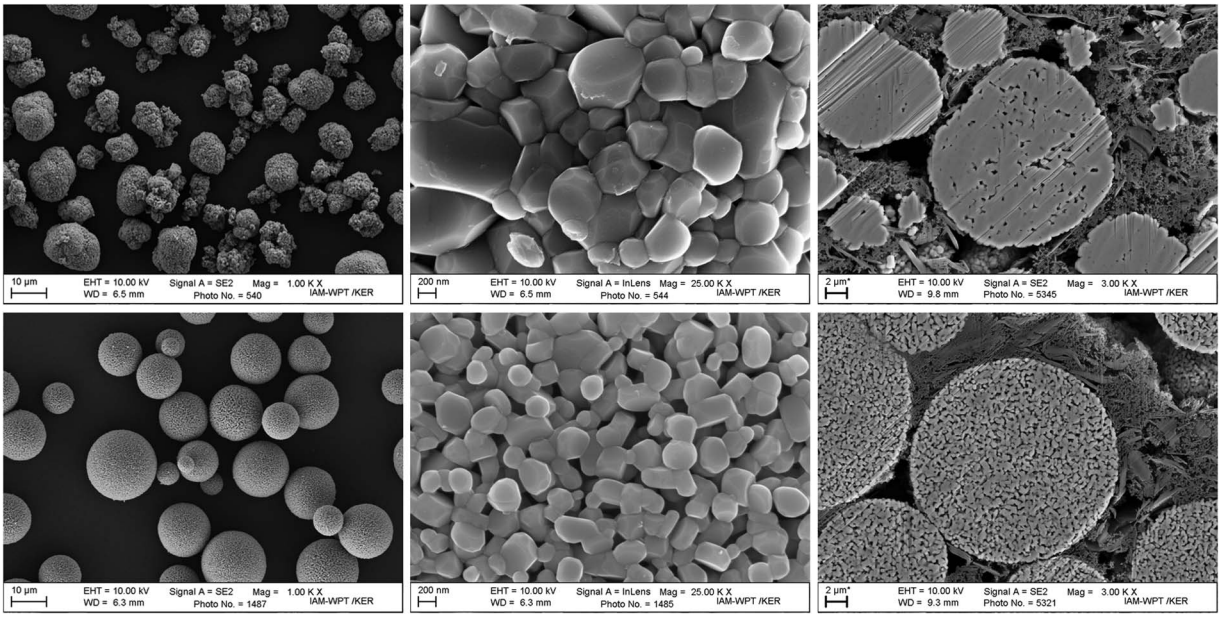

Figure 2. SEM micrographs of p-NCM (top) and n-NCM (bottom) with secondary particles (left), primary particles (middle) and an electrode cross section on the right.

Downloaded on 2019-04-15 to IP 178.251.91.98 address. Redistribution subject to ECS terms of use (see ecsdl.org/site/terms_use) unless CC License in place (see abstract).

Table II. Powder properties of p-NCM and n-NCM.

		Primary particles		Secondary particles			
Material type	Spec. surface area/m^2 g^{-1}	$d_{BET}/\mu m$	$d_{SEM}/\mu m$	$d_{10,3}/\mu m$	$d_{50,3}/\mu m$	$d_{90,3}/\mu m$	Internal porosity secondary particles/%
p-NCM	0.35	3.59	0.83	6.1	9.3	13.9	< 4
n-NCM	2.52	0.50	0.46	10.8	16.4	24.2	40.6

impedance spectroscopy after every 100 load cycles. Details about the measurement procedure are described in the Experimental section.

Fig. 3a shows an exemplary plot of the cell voltage and current curve during one complete load cycle for the battery cell PC-12p, which consist of electrodes with commercial NCM and graphite powders (for cell details see Table I). It is clearly visible that the driving profile includes quick load changes and the cell current is either positive or negative in order to simulate charging or discharging of the car battery. Usually, battery charging in hybrid or electrical vehicles is achieved by energy recuperation such as brake energy recovery or flywheel drive.

In Fig. 3b specific capacity change for charging and discharging during one driving cycle is represented. Furthermore, the sum of both curves is shown, leading to the total specific capacity change. It has a negative sign and therefore the battery loses energy over time, which restricts the possible amount of cycles before recharging.

The complete Common Artemis Urban Driving Cycle load profile starting from SOC90 to SOC10 is shown in Fig. 4 for the tested pouch cell batteries that include different electrode types. The mass loading of the NCM electrodes is 12 mg · cm^{-2} for PC-12p; PC-12n (Fig. 4a) and 24 mg · cm^{-2} for PC-24p; PC-24n (Fig. 4b). The nomenclature PC-xp was chosen to indicate an electrode with p-NCM whereas

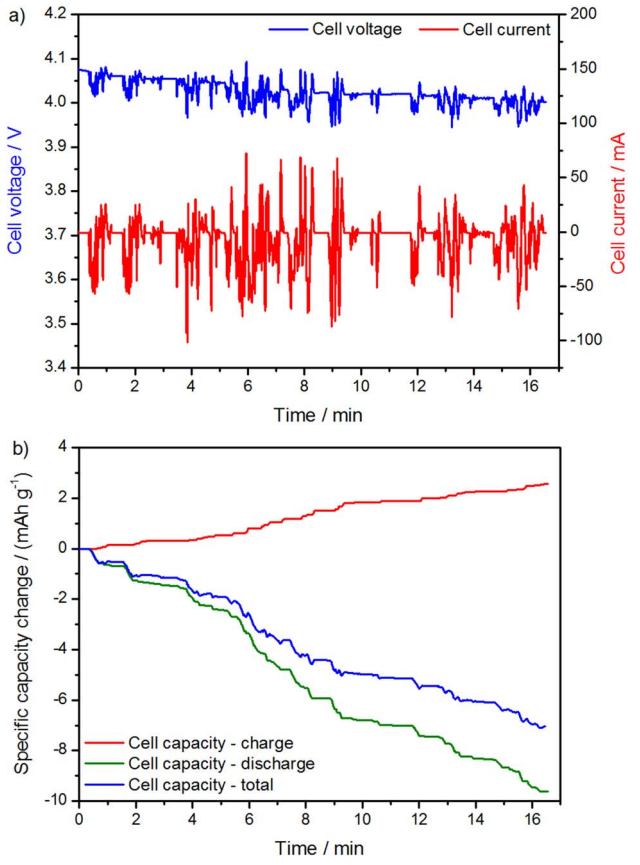

Figure 3. Cell characteristcs for PC-12p during Artemis Urban Driving Cycle test procedure based on SOC90 at t = 0 s. a) Cell voltage and cell current during the test. b) Total cell capacity change subdivided in charge and discharge parts.

PC-xn comprises n-NCM powders. The current is imposed on the cell though the given load profile while the cell voltage is influenced by internal and external electrical resistances. The amount of experimental driving cycles is less than the possible theoretical ones, due to non-ideal behavior of the battery with efficiency clearly below 100%. Table III complements the graphics with detailed information concerning the long-term cycling test.

It is found that the cells with a mass loading of 12 mg · cm^{-2} enable significantly more driving cycles compared to the cells with the double specific mass. Both electrodes have a comparable performance, however the cell that includes the nanostructured cathode material (PC-12n) allows one additional load cycle before the battery has to be recharged. It seems that this difference has its origin mainly from the slightly higher specific capacity. This effect is a direct consequence of the structural electrode set-up as introduced in the Experimental section. Nanostructured electrodes demonstrate a lower internal resistance and have therefore a slightly lower ohmic drop if the cell is under load conditions. This leads to a lower cell potential and a broader capacity window since the maximum charge voltage of 4.2 V is only reached at a higher cell capacity. Therefore, the nanostructured electrode shows a noticeable benefit compared to the conventional electrode. Because the same capacity window (SOC90–SOC10) is used for all cells, the nanostructured electrode material will probably be stressed more than the comparable p-NCM. This seems to be the main reason that nanostructured cells show a higher SOH decrease (see Table IV) in comparison with the p-NCM material, especially at test begin. However, more detailed information requires evaluation of the impedance spectroscopy studies and post mortem examinations.

For the battery cells PC-24p and PC-24n, the similar effect regarding the structure type of the electrode is visible: the cell with nanostructured NCM allows significantly more load cycles than the cell with unmodified electrode material. However, the difference for the 24 mg · cm^{-2} is considerably higher than for the other two cells. In this case, the strong difference in the amount of possible driving cycles could be associated to an extraordinary overall battery resistance in case of PC-24p. The reason for this will be discussed later. The higher overall cell resistance leads to a clear difference in the ohmic drop under load conditions, which in turn leads to heat losses caused by the lower electrical efficiency. As the current is identical for both cells given by the load profile, the effect is in consequence visible on the cell voltage of PC-24p, where the amplitude is considerably higher compared to PC-24n.

Beside the difference among both 24 mg · cm^{-2} cells, less driving cycles are possible in comparison to the cells with less specific mass (12 mg · cm^{-2}) electrodes. As the specific capacity per gram is nearly the same for all cells (146–159 mAh g^{-1}), the thickness of the cathode layers should be approximately two times higher for the 24 mg · cm^{-2} cells (see Table I). During the driving cycles, the load profile is scaled up by a factor of two for the higher capacity cells in order to stress the cells in a comparable way. In theory, the same amount of driving cycles should be possible in consequence. As this is obviously not the case, the described deviations must be caused by the electrode thickness. In general, there is a relationship between the ohmic cell resistance and the cell voltage variations by virtue of the Ohm's law. If the current of the load profile is constant, the amplitude of the cell voltage depends on the overall cell resistance as follows: the higher the cell resistance, the higher is the cell voltage amplitude within load cycling. In consequence, higher cell capacities correlate with higher ohmic cell resistances, if the specific capacity of the active material layer is the same.[13] This leads to a noticeable performance loss for

Downloaded on 2019-04-15 to IP 178.251.91.98 address. Redistribution subject to ECS terms of use (see ecsdl.org/site/terms_use) unless CC License in place (see abstract).

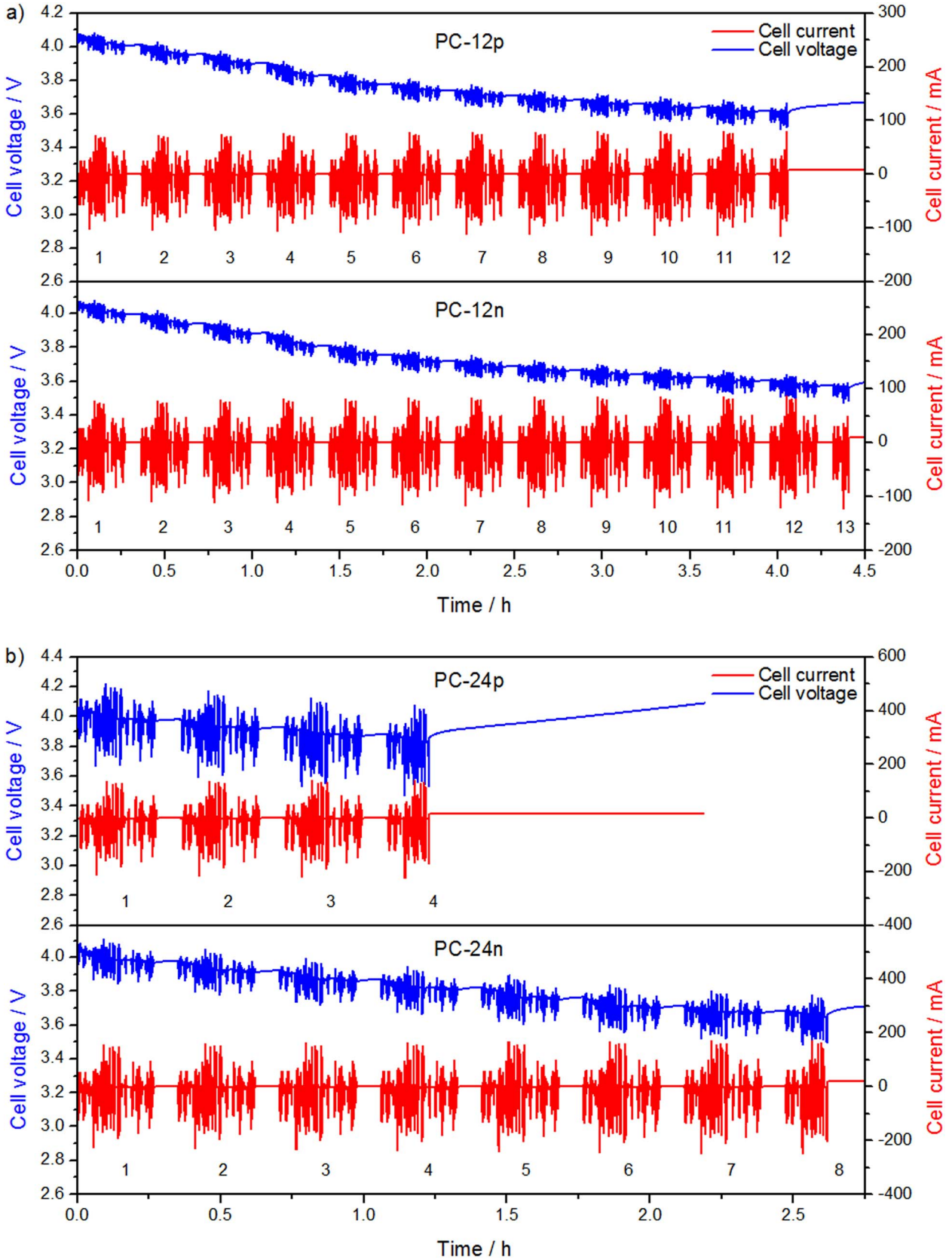

Figure 4. Cell voltage characteristics as a function of Artemis Urban Driving Cycles. The pouche cells are discharging during the test. a) Results for unstructured (PC-12p) and structured (PC-12n) electrodes with 12 mg · cm^{-2} specific weight. b) Electrodes with 24 mg · cm^{-2} specific weight in which PC-24p is the unstructured one.

Downloaded on 2019-04-15 to IP 178.251.91.98 address. Redistribution subject to ECS terms of use (see ecsdl.org/site/terms_use) unless CC License in place (see abstract).

Table III. Technical specifications for different cells used during the Artemis Urban Driving Cycle.

Parameter	Values for PC-12p	Values for PC-24p	Values for PC-12n	Values for PC-24n
Charging time / min	4.06	4.06	4.06	4.06
Discharging time / min	12.50	12.50	12.50	12.50
Rated start capacity / mAh	44.51	87.80	46.46	95.36
Charging capacity / mAh	0.77	1.49	0.82	1.70
Discharging capacity / mAh	–2.89	–5.73	–3.06	–6.43
Resulting capacity / mAh	–2.12	–4.24	–2.24	–4.73
Total charging energy / mWh	3.11	6.09	3.30	6.75
Total discharging energy / mWh	–11.59	–22.13	–12.25	–24.90
Resulting energy / mWh	–8.48	–16.04	–8.95	–18.15
Average charging power / mW	45.92	87.34	47.64	98.20
Average discharging power / mW	–55.60	–106.94	–58.89	–123.57
Resulting average power / mW	–30.72	–58.15	–32.46	–67.22
Capacity SOC90–SOC10 / mAh	36.05	70.24	37.16	76.28
Theoretical amount of full cycles	17 (17.0)	16 (16.6)	16 (16.6)	16 (16.1)
Possible amount of full cycles	11	3	12	7
Cell voltage SOC90 / V	4.05	3.98	4.03	4.00
Cell voltage SOC10 / V	3.45	3.43	3.44	3.43

high energy cells. Furthermore, it is well-known that thick electrodes may age differently than high counterparts with thin electrodes.[13]

Nevertheless, in specific applications the doubled mass loading enables a significant reduction in the required number of cells by about a factor of two if the same battery cell construction is used. This major circumstance is an important benefit in particular for the automotive industry where the space for battery packs is strongly limited and goes to the expense of the usable car volume. Furthermore, high energy cells are an indispensable prerequisite in order to enable long vehicle ranges.

Fig. 5 illustrates the specific capacity as a function of the driving cycles, whereby the respective battery capacity was determined in a separate experiment after each 100 cycles during discharging from SOC90 to SOC10. Furthermore, the corresponding driving distance is indicated by an extra axis on top of the diagram. One load cycle is equivalent to a driving distance of 4.87 km. The experiment was carried out up to 8000 cycles. The data above 8000 cycles is gained through linear extrapolation (dotted lines). Table IV includes associated information of the state of health level depending on the load cycles.

The specific capacities of PC-12n and PC-24n cells with nanostructured electrodes are significantly higher compared to cells with p-NCM materials. The curve characteristics for the first-mentioned cells are always better during the complete experiment, which clearly indicates a benefit with nanostructured electrodes. And even the SOH values of the cells with nanostructured material, which are decreasing significantly in the beginning, converge to the SOH values of the cells with p-NCM with increasing driving cycles.

The reason why structured electrodes have a higher specific capacity is a morphological phenomenon. BET measurements show that the accessible surface area is higher for the n-NCM powder. Furthermore, the n-NCM powder has an open porosity and this ensures a better wettability relating to penetration through the electrolyte, and thus the diffusion paths in the cathode material are shorter. Thereby, the cells with n-NCM powder have reduced internal ohmic resistances. Therefore, the material can be utilized better since the respective voltage window is widened. As a result, the specific capacities between SOC90 and SOC10 are higher.

Based on the hypothetic data through the extrapolation (see Fig. 5), there is a point of intersection at about 10000 cycles where the specific capacities of the cells with 12 mg · cm^{-2} electrodes fall below the values of the 24 mg · cm^{-2} cells, no matter which kind of cathode material is used. Since the cathode material is not the crucial factor, the reason for the described effect has to be associated with the electrode thickness of cathode or anode. Cells with 24 mg · cm^{-2} electrodes have an increased internal ohmic resistance compared to the 12 mg · cm^{-2} cells. The higher internal ohmic resistance leads to a higher ohmic drop and therefore to a higher cell voltage amplitude during load cycling. The resulting capacity window in the voltage range of 4.2 to 3.0 V under test conditions is consequently a little bit narrower, which ensures that the cells will overall be a little less stressed with increasing driving cycles. Therefore, the cells exhibit a slightly better

Table IV. State of health development as a function of Artemis Urban Driving Cycles.

Artemis Urban Driving Cycles	SOH for PC-12p/%	SOH for PC-24p/%	SOH for PC-12n/%	SOH for PC-24n/%
0	100	100	100	100
1000	97.0	95.3	95.0	93.6
2000	94.8	92.8	93.0	91.8
3000	93.2	91.8	91.7	90.4
4000	91.5	90.8*	90.5	89.8
5000	90.0	—	89.4	89.3
6000	89.2	90.0	88.8	88.6
7000	88.4	89.6	88.0	88.3
8000	87.5	89.0	87.3	87.9

*3900 cycles.

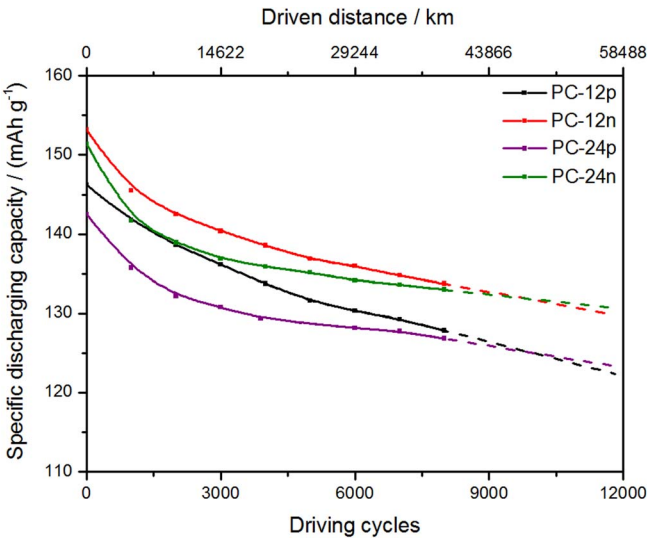

Figure 5. Specific discharging capacity characteristics as a function of the number of Artemis Urban Driving Cycles. The second x-axes shows the corresponding driven distance.

Downloaded on 2019-04-15 to IP 178.251.91.98 address. Redistribution subject to ECS terms of use (see ecsdl.org/site/terms_use) unless CC License in place (see abstract).

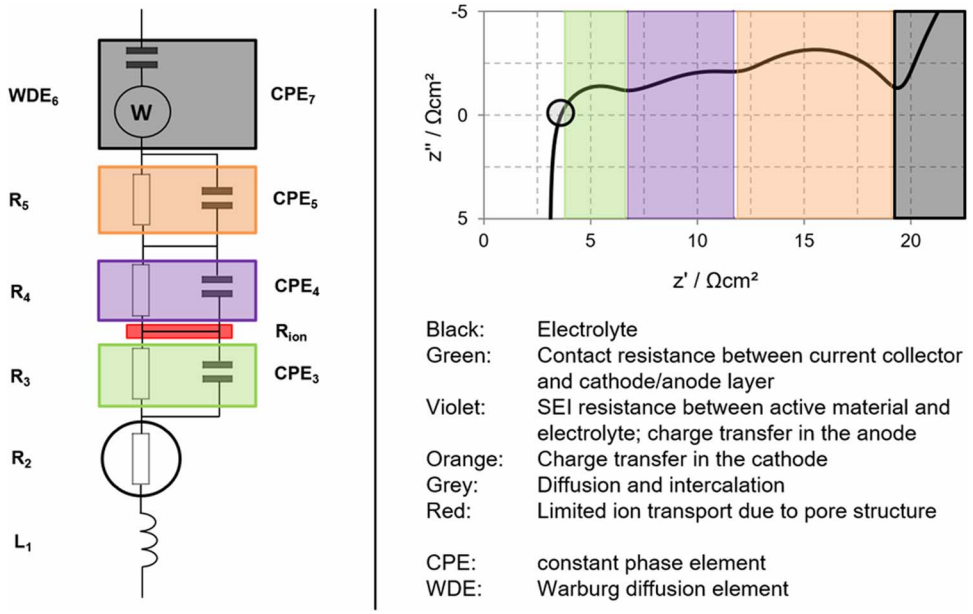

Figure 6. Schematic equivalent circuit for a complete battery cell. Furthermore, a corresponding electrochemical impedance spectrum is shown. Individual contributions to the spectrum are marked with colored retangles and are explaned in the legend.

aging behavior compared to the cells which include 12 $mg \cdot cm^{-2}$ electrodes.

Electrochemical impedance spectroscopy is a useful tool in order to investigate material ageing of battery components to understand the degradation mechanisms that limit the lifetime.[14] Therefore, simulations of the battery behavior were carried out by using equivalent circuits.[15] Thereby, it is attempted to represent all important battery components by ohmic resistances, coils and capacitors (Fig. 6). In particular, the individual contributions to the simulated spectrum are: L_1, R_2, R_3, CPE_3, R_{ion}, R_4, CPE_4, R_5, CPE_5, WDE_6 and CPE_7. "L" symbolizes a coil, "R" an ohmic resistance, CPE a constant phase element and finally WDE a Warburg diffusion element.

L_1 is used to simulate the cables and the cell inductance. R_2 and R_{ion} are summarizing the ohmic contributions of electronic and ionic charge transport phenomena in all cell components, whereby R_2 stands for the electrolyte resistance.

Three RQ-elements are necessary to describe the polarization processes. The RQ-element is a combination of an ohmic resistance R and a not ideal capacitor CPE in parallel since a clear RC behavior could rarely be observed in a real electrochemical system.[16] The RQ-element is also known as ZARC-element or Cole-Cole circuit element.[17,18] R_4 and CPE_4 are assigned to the graphite material at the anode, representing a combination of SEI-diffusion and charge transfer at the surface. The RQ-elements 3 (R_3 & CPE_3) and 5 (R_5 & CPE_5) are localized at the cathode. RQ-element 3 is attributed to the contact resistance between cathode and current collector, while element 5 stands for the charge transfer of lithium-ions at the interface cathode/electrolyte.

WDE_6 is an equivalent electrical circuit component that models the diffusion process. Generally, it is associated with a charge-transfer resistance and a double layer capacitance. In this case, it mainly symbols mass transfer processes and intercalation of lithium. Finally, the serial capacity CPE_7 represents the differential capacity of the cell.

The classification of the various contributions to the corresponding battery processes requires DRT (distribution of relaxation times) measurements and analysis. The conclusions of these investigations are already published in literature.[19] The complete equivalent circuit is demonstrated in Fig. 6.

Fig. 7 shows the results of the impedance spectroscopy simulations with the above introduced equivalent electrical circuit. For further discussion, it has to be pointed out that the anode materials are the same for cells with the same specific weight, regardless of whether an electrode with pristine or with nanostructured cathode is implemented. The black curves (squared measuring points) illustrate the ohmic contributions R_2 in terms of specific electrolyte resistances r_2, taking into account that the electrode surface is 25 cm^2. For all four cells, the electrolyte resistances lie in the region of 2–3 $\Omega \cdot cm^2$, if some slips are neglected. Furthermore, the resistances increase linearly during cycling, but the changes are not too large and have only a low influence in the impedance spectra. This behavior could be conclusively explained through the decomposition of the electrolyte components (mixture of different electrolytes, conducting salt and additives) or due to the electrolyte consumption during the SEI formation at the anode. Both negative impacts lead to a decreasing electrolyte and conducting salt concentration and therefore to an increased ohmic resistance over the time. Furthermore, the lithium salt significantly affects the interfacial resistance because it affects the reactions of the electrolyte with the electrode.[20] It is also known in literature that the lithium salt concentration greatly influences the capacity, rate capability and cycle life of the electrode.[21]

The specific resistance through the pore structure r_{ion} reveals a similar picture (red curves with dotted measuring points): the resistance slightly increases with a linear characteristic, whereby the effect is somewhat higher for both nanostructured materials. It seems that general morphological differences of the pristine and the nanostructured active material, especially the pore characteristics (see Table II), are responsible for the difference in impedance behavior. As r_{ion} stands for the ion transport limitation in the pore structure, a plausible explanation could be marginal accelerated electrolyte degradation which causes a higher viscosity of the electrolyte or a decreased conductions salt concentration in the nanostructured pore system. Such adverse electrolyte alteration can limit the ion transport in the pore system which correlates to a higher charge transfer resistance.

The violet curves (stars as data points) represent the development of the graphite anode resistances, more precisely the SEI formation and the charge transfer reaction, which is a surface process at the electrode. The specific resistances r_4 are considerably high at the beginning of the load cycling test and decrease relatively quickly over the timer following an exponential function. This observed effect could be attributed to SEI formation since the surface layer at the boundary layer electrode/electrolyte optimizes the necessary lithium-ion desolvation process when lithium intercalates in graphite bulk material.

Downloaded on 2019-04-15 to IP 178.251.91.98 address. Redistribution subject to ECS terms of use (see ecsdl.org/site/terms_use) unless CC License in place (see abstract).

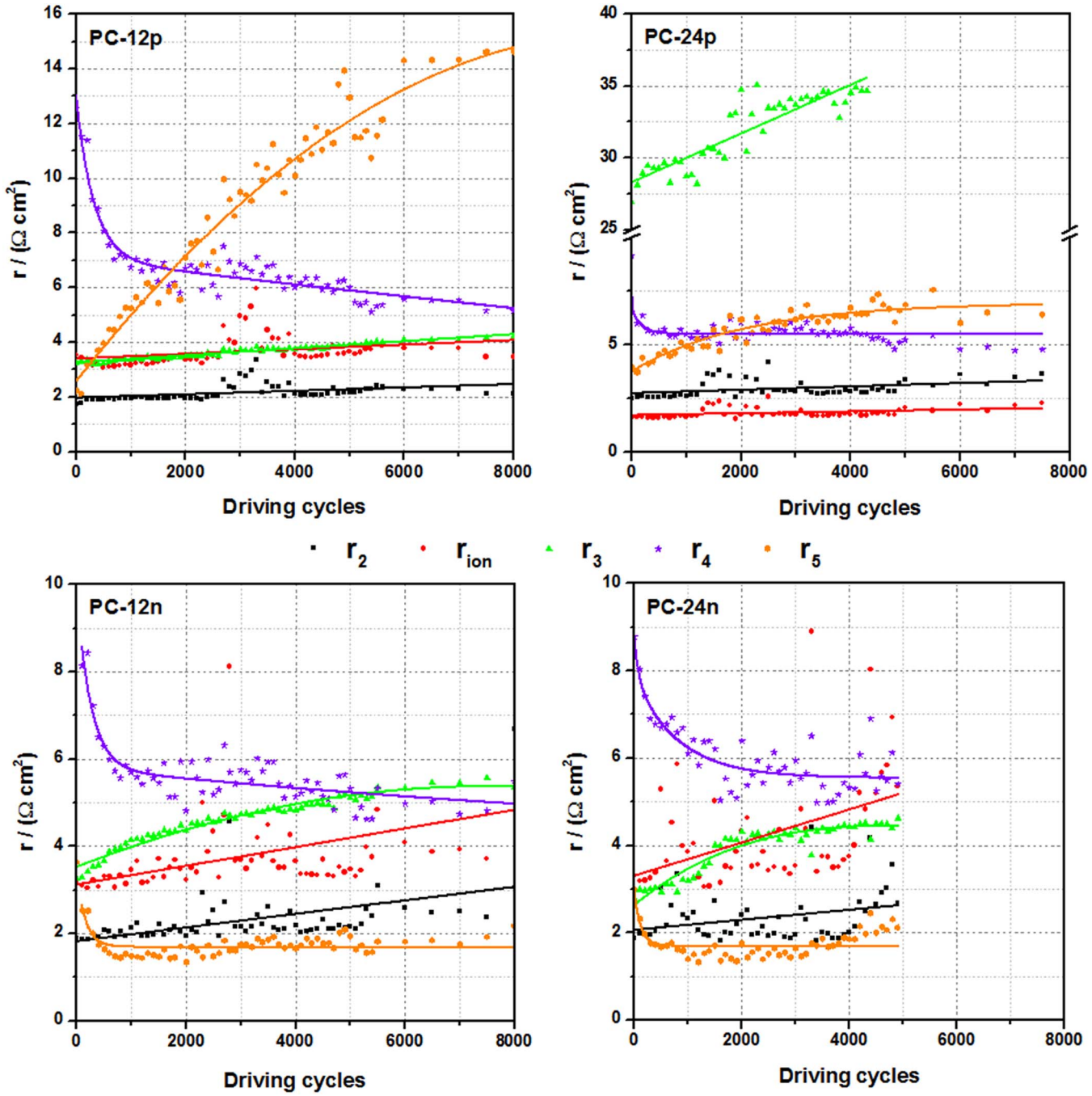

Figure 7. Specific resistances r_2 (black), r_3 (green), r_4 (violet), r_5 (orange) and r_{ion} (red) for all four cells with 25 cm^2 electrode surface area.

In consequence, the resistance is decreasing. At the latest after 2000 cycles a linear behavior could be recorded for all cells. In case of the cells with a specific weight of 12 $mg \cdot cm^{-2}$, a decreasing resistance during further cycling is observed, while the electrodes with a higher mass loading demonstrate a constant value. Obviously, the thick, more porous anode electrodes (see Table I) show a much faster break-in behavior. A possible reason is that SEI formation is completed faster for these electrodes because the electrolyte can penetrate the pore system more easy and surface wetting is therefore much faster, which enhances the SEI formation.[22]

R_3 is part of the RQ-element 3 and stands for the contact resistance between cathode electrode and current collector. The green curves (triangular data points) show that a linear behavior with a slightly increasing resistance is observed for unstructured cells. There is no evidence for an exfoliation of the active electrode material from the aluminum foil for the unstructured material caused by load cycling. However, the PC-24p cell exhibits an extremely high ohmic resistance from the very beginning which is caused by the preparation conditions. In order to obtain the same volumetric loading densities, the electrodes with p-NCM powders were not compacted after drying. While this seems to have no effect to the resistance of the thin electrode, the influence of missing post-compaction for the thick p-NCM electrode appears to be very pronounced. However, the relative changes during increasing number of driving cycles are again comparable.

Cells including nanostructured electrode materials show an exponential resistance increase with a linear approach after approximately 3000 load cycles. The observed exponential behavior, in particular at test begin, is probably caused by loss of contact between active and

Downloaded on 2019-04-15 to IP 178.251.91.98 address. Redistribution subject to ECS terms of use (see ecsdl.org/site/terms_use) unless CC License in place (see abstract).

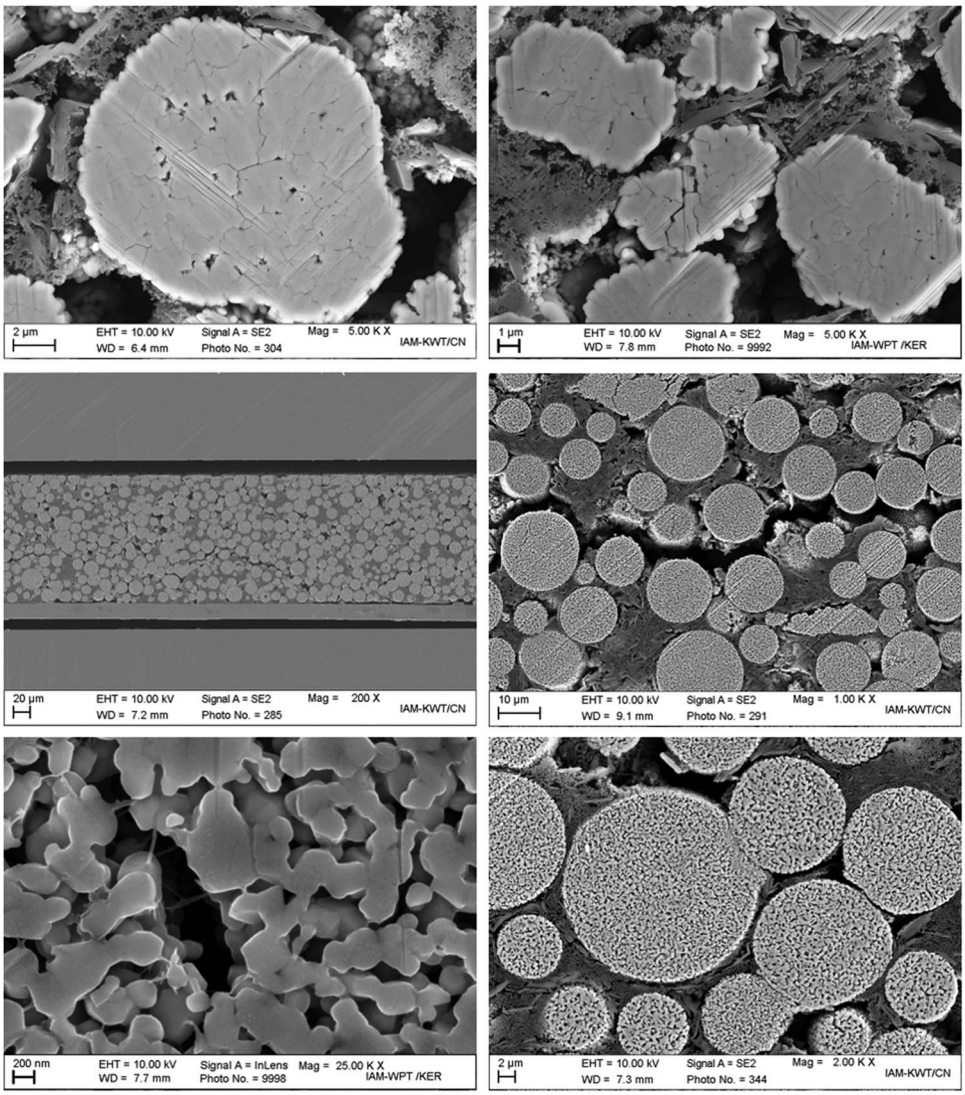

Figure 8. Post-mortem SEM micrographs after the load cycling experiment of electrodes with pristine NCM materials (top) and with nanostructured NCM materials (middle, bottom).

inactive components as well as between the cathode layer and the current collectors. The post-mortem micrographs (see Fig. 8 middle) indicate that exfoliation between the inactive components of the active material and the aluminum foil of the nanostructured electrodes is present. A possible reason for the contact loss is that binder migrates into the granulate (Fig. 8 bottom, left) which lead to decreasing adhesion properties to the aluminum foil or within the electrode materials.[23] This clearly shows that the optimized preparation instruction for p-NCM powder cannot be simply transferred to the nanostructured powder, such as it has been done here.

The opposite behavior could be monitored for R_5 which represents charge transfer of lithium ions inside the material (orange curves with hexagonal measuring points). In this case, both pristine electrodes show an exponential curve, whereby the cells with nanostructured NCM materials provide a linear behavior, apart from the relatively quick running-in phase, where the resistances are decreased by 50% within the first 500 driving cycles.

In principle, structural changes of the active material or cracks in the active material can lead to an increase in the r_5 resistance. The post-mortem analysis via XRD (X-ray diffraction) does not exhibit any changes in the lattice structure before and after cycling and moreover the formation of impurity phases can be excluded, too. Therefore, if present, changes have to occur at a microscopic or mesoscopic level. SEM images (Fig. 8, bottom right) show no evidence for crack formation in the nanostructured electrode and therefore no essential impedance change is expected which is in accordance with the EIS results that are presented at this point. On the other side, some cracks are obviously formed during cyclical aging in the pristine NCM material. These kinds of cracks are able to compromise the electronic and ionic conductivity inside the particles and cause transport barriers for electrons and lithium-ions leading to an increasing ohmic resistance over the time.[24] This can even result in complete contact losses with accompanied inactivity of some parts of the electrodes.[24] Such mechanical damage contributes to capacity losses by inactive regions and new surface formation, which consume lithium-ions for the formation of additional solid electrolyte interface (SEI).[24] Furthermore, Kandrakov et al. have recently reported that accelerated aging of NCM materials is related to the disintegration of secondary particles caused by intergranular fracture, which is an effect of mechanical stress at the interfaces between the primary crystallites.[25]

Conclusions

The research activity of this work has concentrated on the evaluation of a novel nanostructured NCM electrode material that is processed in-house originating from a commercial available

Downloaded on 2019-04-15 to IP 178.251.91.98 address. Redistribution subject to ECS terms of use (see ecsdl.org/site/terms_use) unless CC License in place (see abstract).

$LiNi_{0.33}Co_{0.33}Mn_{0.33}O_2$ standard material powder. To test the resulting material properties, different types of pouch cells with pristine and derived nanostructured active material were stressed in a long-term load cycling test by applying Artemis Urban Driving Cycles. To investigate the capacity loss of the cells due to load cycling and calendar aging, electrochemical impedance spectroscopy and post-mortem analysis were used.

The aim of this work was to improve any NCM standard material with a post-synthesis process to optimize the granule size distribution and particle shape in order to enhance the cathode active material of pouch cells regarding their capacity and cyclic stability.

In general, the results demonstrate that the nanostructured electrodes have a higher capacity as they demonstrate a lower internal cell resistance and have therefore a lower ohmic drop under load conditions. It has to be pointed out that the amount of possible load cycles in the long-term test was in every case higher for the nanostructured electrodes, regardless of the mass loading (12 or 24 $mg \cdot cm^{-2}$) of the active material and therefore of the electrode thickness. The obtained slightly less favorable SOH behavior of the nanostructured electrodes can be closely associated with the higher material stress caused by a broader capacity window between the defined maximum charging and minimum discharging voltage (4.2 and 3.0 V) that corresponds to a higher amount of performed load cycles. However, the impedance spectroscopy results also show that, especially at the beginning, the contact loss of the cathode layer to the current collector is strongly pronounced for cells with nanostructured NCM materials.

Summarizing the results, post-processing of the electrode active material is a relatively simple method to improve the properties of lithium-ion electrode materials, especially regarding high energy applications and lifetime optimization.

The following conclusions and recommendations for further research activities may be drawn:

- As post-mortem SEM micrographs exhibit exfoliation between active and inactive electrode components as well as the cathode layer and the aluminum foil, the adhesion properties should be improved. One promising starting point is to change the binder or its composition in order to prevent binder migration into the granulate which finally increases the contact resistance between electrode and current collector.
- Additional tests with other promising cathode materials, e.g. NCM-622 or NCM-811, should be performed.
- It seems to be possible to transfer the introduced processing method for cathode materials to anode electrode materials.

Acknowledgments

The authors thank our former DLR colleague Johannes Sattler for performing the load cycling and electrochemical impedance spectroscopy tests. Dirk Schneider (DLR) and Sven Glatthaar (formerly KIT) are gratefully acknowledged for helpful discussions and experimental support. The presented experiments were carried out in the frame of the theme "Elektrochemische Speicher im System – Zuverlässigkeit und Integration" within the research portfolio of the Helmholtz Association of German Research Centres (HGF).

ORCID

Andreas M. Dreizler https://orcid.org/0000-0003-2681-6350
Norbert Wagner https://orcid.org/0000-0002-2596-8689

References

1. K. Young, C. Wang, L. Y. Wang, and K. Strunz, in *Electric Vehicle Integration into Modern Power Networks*, ed. R. Garcia-Valle and J. Peças Lopes, Springer, New York, NY, (2013), Chapter 2: Electric Vehicle Battery Technologies, Power Electronics and Power Systems. Springer, New York, NY, 15.
2. J. M. Tarascon and M. Armand, *Nature*, **6861**, 359 (2001).
3. N. Nitta, F. Wu, J. T. Lee, and G. Yushin, *Mater. Today*, **18**, 252 (2014).
4. X. Xu, S. Lee, S. Jeong, Y. Kim, and J. Cho, *Mater. Today*, **16**, 487 (2013).
5. C. Julien, A. Mauger, K. Zaghib, and H. Groult, *Materials*, **9**, 595 (2016).
6. M.-J. Uddin, P. K. Alaboina, and S.-J. Cho, *Mater. Today Energy*, **5**, 138 (2017).
7. K. M. Shaju and P. G. Bruce, *Adv. Mater*, **18**, 2330 (2006).
8. M. André, "Real-world driving cycles for measuring cars pollutant emissions", Part A: The ARTEMIS European driving cycles, Report INRETS-LTE 0411, (2004).
9. M. André, *Sci. Total Environ.*, **334–335**, 73 (2004).
10. M. André, R. Joumard, R. Vidon, P. Tassel, and P. Perret, *Atmos. Environ.*, **40**, 5944 (2006).
11. Common Artemis Driving Cycles (CADC), https://www.dieselnet.com/standards/cycles/ artemis.php, (accessed November 2017).
12. S.-C. Yin, Y.-H. Rho, I. Swainson, and L. F. Nazar, *Chem. Mater*, **18**, 1901 (2006).
13. Y. Leng, S. Ge, D. Marple, X.-G. Yang, C. Bauer, P. Lamp, and C.-Y. Wang, *J. Electrochem. Soc.*, **164**, A1037 (2017).
14. U. Tröltzsch, O. Kanoun, and H.-R. Tränkler, *Electrochim. Acta*, **51**, 1664 (2006).
15. L. Wang, J. Zhao, X. He, J. Gao, J. Li, C. Wan, and C. Jiang, *Int. J. Electrochem. Sci.*, **7**, 345 (2012).
16. J. R. Macdonald, *Solid State Ionics*, **13**, 147 (1984).
17. J. R. Macdonald, *Solid State Ionics*, **15**, 159 (1985).
18. K. S. Cole and R. H. Cole, *J. Chem. Phys.*, **9**, 341 (1941).
19. J. Illig, *Physically based Impedance Modelling of Lithium-Ion Cells*, KIT Scientific Publishing, Karlsruhe, (2014).
20. Q. Li, J. Chen, L. Fan, X. Kong, and Y. Lu, *Green Energy Environ.*, **1**, 18 (2016).
21. N. Wongittharom, C.-H. Wang, Y.-C. Wang, G. T.-K. Fey, H.-Y. Li, T.-Y. Wu, T.-C. Lee, and J.-K. Chang, *J. Power Sources*, **260**, 268 (2014).
22. G. M. Veith, M. Doucet, J. K. Baldwin, R. L. Sacci, T. M. Fears, Y. Wang, and J. F. Browning, *J. Phys. Chem. C*, **119**, 20339 (2015).
23. S. Jaiser, M. Müller, M. Baunach, W. Bauer, P. Scharfer, and W. Schabel, *J. Power Sources*, **318**, 210 (2016).
24. R. Hausbrand, G. Cherkashinin, H. Ehrenber, M. Gröting, K. Albe, C. Hess, and W. Jaegermann, *Mater. Sci. Eng., B*, **192**, 3 (2015).
25. A. O. Kondrakov, A. Schmidt, J. Xu, H. Geßwein, R. Mönig, P. Hartmann, H. Sommer, T. Brezesinski, and J. Janek, *J. Phys. Chem. C*, **121**, 3286 (2017).

Downloaded on 2019-04-15 to IP 178.251.91.98 address. Redistribution subject to ECS terms of use (see ecsdl.org/site/terms_use) unless CC License in place (see abstract).